

## Deep learning–based nondestructive evaluation of reinforcement bars using ground-penetrating radar and electromagnetic induction data

Li, Xiaofeng; Liu, Hai; Zhou, Feng; Chen, Zhongchang; Giannakis, Iraklis; Slob, Evert

**DOI**

[10.1111/mice.12798](https://doi.org/10.1111/mice.12798)

**Publication date**

2021

**Document Version**

Final published version

**Published in**

Computer-Aided Civil and Infrastructure Engineering

**Citation (APA)**

Li, X., Liu, H., Zhou, F., Chen, Z., Giannakis, I., & Slob, E. (2021). Deep learning–based nondestructive evaluation of reinforcement bars using ground-penetrating radar and electromagnetic induction data. *Computer-Aided Civil and Infrastructure Engineering*, 37 (2022)(14), 1834-1853. <https://doi.org/10.1111/mice.12798>

**Important note**

To cite this publication, please use the final published version (if applicable). Please check the document version above.

**Copyright**

Other than for strictly personal use, it is not permitted to download, forward or distribute the text or part of it, without the consent of the author(s) and/or copyright holder(s), unless the work is under an open content license such as Creative Commons.

**Takedown policy**

Please contact us and provide details if you believe this document breaches copyrights. We will remove access to the work immediately and investigate your claim.

***Green Open Access added to TU Delft Institutional Repository***

***'You share, we take care!' - Taverne project***

**<https://www.openaccess.nl/en/you-share-we-take-care>**

Otherwise as indicated in the copyright section: the publisher is the copyright holder of this work and the author uses the Dutch legislation to make this work public.



# Deep learning–based nondestructive evaluation of reinforcement bars using ground-penetrating radar and electromagnetic induction data

Xiaofeng Li<sup>1</sup> | Hai Liu<sup>2</sup> | Feng Zhou<sup>1</sup> | Zhongchang Chen<sup>1</sup> | Iraklis Giannakis<sup>3</sup> | Evert Slob<sup>4</sup>

<sup>1</sup> School of Mechanical Engineering and Electronic Information, China University of Geosciences (Wuhan), Hubei, China

<sup>2</sup> School of Civil Engineering, Guangzhou University, Guangdong, China

<sup>3</sup> School of Geosciences, University of Aberdeen, Scotland, UK

<sup>4</sup> Department of Geoscience & Engineering, Delft University of Technology, Zuid-Holland, The Netherlands

## Correspondence

Feng Zhou, School of Mechanical Engineering and Electronic Information, China University of Geosciences (Wuhan), Hubei, China.

Email: [zhoufeng@cug.edu.cn](mailto:zhoufeng@cug.edu.cn)

## Funding information

National Natural Science Foundation of China, Grant/Award Numbers: 41974165, 42111530126; Hubei Key Laboratory of Intelligent Geo-Information Processing, Grant/Award Number: KLIGIP-2018A2

## Abstract

This paper proposes a nondestructive evaluation method based on deep learning using combined ground-penetrating radar (GPR) and electromagnetic induction (EMI) data for autonomic and accurate estimation of the cover thickness and diameter of reinforcement bars. A real-time object detection algorithm—You Only Look Once–version 3 (YOLO v3)—is adopted to automatically identify the reinforcement bar reflected signals from radargrams, with which the range of the cover thickness is roughly predicted. Subsequently, EMI data, accompanied with the cover thickness range, are imported to a one-dimensional convolutional neural network (1D CNN), pretrained by calibrated EMI and GPR data, to simultaneously estimate the cover thickness and reinforcement bar diameter. Testing with the on-site GPR data shows that YOLO v3 is superior to Single Shot Multi-box Detector method in GPR hyperbolic signal identification. Testing of 1D CNN with the EMI and GPR data collected in an in-house sand pit experiment shows that the estimation accuracy of the cover thickness and reinforcement bar diameter is, respectively, 96.8% and 90.3% with a permissible error of 1 mm. Further, an experiment with concrete specimens demonstrates that among the 22 estimated values (including the reinforcement bar diameter and cover thickness), there are 17 values accurately estimated, while the inaccurately estimated values have an error up to 2 mm. The experimental results show that the proposed method can autonomously evaluate the reinforcement bar diameter and cover thickness with a high accuracy.

## 1 | INTRODUCTION

In civil and infrastructure engineering practice, it is of great importance to inspect and estimate the quality of the reinforced concrete after its construction (Leet & Bernal, 1982; Taheri, 2019). According to conventional supervi-

sion and acceptance standards, in the stage of project acceptance, some crucial properties of the reinforcement bars, for instance, the diameter and cover thickness, are required to be strictly examined (Hai et al., 2002). Nondestructive testing (NDT), including electrical and sonic methods, has been frequently used for noninvasive



estimation of construction details (Forde et al., 2013). However, to date, some significant challenges still exist in the practical estimation of reinforced concrete, especially in quantitative characterizations of details. On the one hand, a high estimation accuracy, up to an order of 1 mm, is required when inspecting the reinforcement bar diameter and cover thickness (Zhang et al., 2019); on the other hand, intelligent data processing and interpretation are required for rapid on-site testing and estimation (Kim et al., 2021).

In concrete reinforcement inspection, cover meter is a frequently used commercial NDT instrument because it is highly sensitive to metal targets, low-cost, and trivially deployable (Rathod et al., 2019). Cover meters are based on electromagnetic induction (EMI). Under the excitation of time-varying current, a conductive object induces a secondary magnetic field, whereas concrete, as a nonferromagnetic background material, does not induce eddy current and thus contributes nothing to the secondary magnetic field (Xiao et al., 2017). The intensity distributions of the received secondary fields are dependent on the geometric properties and the compositions of the conductive objects. Therefore, the cover thickness and diameter of the reinforcement bars are able to be estimated by the EMI responses once a wide range of properties of reinforcement bars are exactly calibrated by the cover meters. However, there exist multiple solutions for certain sets of EMI responses. In practice, by referring to the construction drawings or digging test, the diameter of reinforcement bar is preset as the prior knowledge to accurately estimate the cover thickness, or vice versa (Forde et al., 2013). However, the prior knowledge is not always available. A solution was proposed that can simultaneously derive the reinforcement bar diameter and cover thickness by deploying two spaced receiving coils to obtain two sets of EMI readings at different distances (Alldred, 1995). However, the scheme makes the instrument structure sophisticated, and the mutual interference between the coils is unavoidable. Quek et al. (2003) established a curvilinear model to estimate the reinforcement diameter and cover thickness by extracting the peak amplitude and the full width at half height (FWHH) from the measured EMI curves. Their results show that, at a given diameter of the reinforcement bar, the relative error of the estimated cover thickness is  $\pm 5\%$ ; whereas when the diameter is unknown, the relative error of the estimated cover thickness reaches  $\pm 10\%$ , implying that the estimation accuracy depends on prior knowledge.

Ground-penetrating radar (GPR) is another commercial NDT technology that has been widely applied in various fields of civil and infrastructure engineering. It utilizes wideband antennas to transmit high-frequency (tens to thousands of megahertz) electromagnetic (EM) waves, and records the echoes to infer the information of the targets in the background material media (Lai et al., 2018). GPR

has been successfully applied to pavement defect examination (Zhang et al., 2020), bridge deck monitoring (Belli et al., 2008), urban underground pipeline detection (Prego et al., 2017), and so on. In particular, GPR has been applied to examine the reinforced concrete due to the great conductivity contrast between the concrete and the steel bars. In the concrete inspection, the GPR instrument is moved on the surface of the concrete in a straight path, collecting multiple traces of echoes from the bars (Lai et al., 2018). The formed radargrams result in some signatures similar to hyperbolic curves, which are caused by the strong reflected waves from the cylindrical targets. The hyperbolic signals are treated as key signatures for reinforcement bar detection (Lei et al., 2019). However, the hyperbolic signals are unable to straightforwardly quantify the properties of the inspected reinforcement bars. As a result, it is significant to process the hyperbolic signals in the radargrams before the quantitative interpretation. Conventional data processing techniques include time-zero correction, direct wave removal, filtering, and migration, however, interpretation remains manual and heavily relies on the experience of the practitioners (Jol, 2008). Some image processing methods, including curve fitting and Hough transform, have been applied to extract the hyperbolic signals from the radargrams (Ristic et al., 2009; Windsor et al., 2013). The disadvantages of these methods are that a template of curve fitting has to be prepared in advance and the computation cost is high. Some postprocessing algorithms have also been applied to process hyperbolic signals. Dou et al. (2016) proposed a postprocessing method that uses the column-connection clustering algorithm to segment the hyperbolic signals in radargrams from the background. Further, X. Zhou et al. (2018) proposed an improved algorithm, called open-scan clustering, to evaluate buried pipes based on the features of the downward opening of hyperbolic signals. To obtain the cover thickness, the wave velocity (corresponding to the permittivity of the background material) needs to be accurately acquired (Sham & Lai, 2016). However, the wave velocity is usually evaluated by experience, which unavoidably brings errors in the interpretation. Liu and Sato (2014) developed a multiple offset array GPR system and conducted a common-source measurement to improve the precision of the velocity evaluation in estimating pavement thickness. When estimating the reinforcement bar properties with GPR, the reinforcement bar diameter is smaller than the working wavelength of GPR in the general reinforced concrete circumstances (Jazayeri et al., 2019). Consequently, the features of the hyperbolic signals are not sufficiently sensitive to the diameter of the reinforcement bars. Sensitivity analyses based on the in-house GPR measurements proved that it is difficult to acquire accurate estimation of the diameter of reinforcement bars using GPR hyperbolic signals (Wiwatrojanagul et al., 2017). Therefore, estimating the cover thickness and



diameter of reinforcement bars is particularly challenging using GPR, with no conclusive and universal interpretation methods to this day.

A combination of GPR and EMI sensing techniques can compensate for the respective limitations of the two methods, and it has been successfully applied in landmine detection (Sato et al., 2018), underground historical site exploration (Saey et al., 2014), and soil water content assessment (Barca et al., 2019). In concrete inspection, a combined EMI and GPR framework is expected to reduce the dependence of EMI data on prior information. In our previous work, a novel prototype has been developed that combines GPR and EMI in a compact box (hereinafter referred to as dual-sensing prototype). The developed system is capable of simultaneously collecting EMI and GPR data in a single scanning measurement (F. Zhou et al., 2018). However, the manual interpretation is time-consuming and labor-intensive, which dramatically increases the costs for the practical applications in building sites. Therefore, developing an efficient and automatic data processing and interpretation method is of significance for the NDT community (Liu et al., 2020).

In the recent decades, machine learning has attracted significant interest in a wide range of fields, including civil and infrastructure engineering (Amezquita-Sanchez et al., 2016). There have been some reports on the successful applications of machine learning techniques to concrete quality evaluation (Rafiei et al., 2017; Valikhani et al., 2021), bridge crack inspection (Okazaki et al., 2020), and estate sales price prediction (Rafiei & Adeli, 2016). Meanwhile, as an important subset of machine learning, deep learning, featured with multiple layers of neural network architecture to solve some complex problems, is becoming the current study hotspot as high-performance computing and big data become more trivially accessible (Feng et al., 2017). Zhang et al. (2021) applied generative adversarial network to impute link travel times with trajectory data; Hu et al. (2021) used a modified recursive binary tree network to reconstruct 3D bridge structure; Maeda et al. (2021) used generative adversarial network for road damage detection; Guo et al. (2021) proposed a semisupervised learning-based convolutional neural network (CNN) to classify architectural appearance defects from image data; Sajedi et al. (2021) used deep Bayesian neural networks for vision-based structural inspections. These studies demonstrate promising prospects of deep learning applications to civil and infrastructure engineering.

In terms of GPR data interpretation, Wang et al. (2020) proposed a method using genetic algorithm to semiautomatically identify the buried reinforcement bars using solely GPR data. The results show that the missed detection rate and false alarm rate are, respectively, 11.98% and

9.08%. Lei et al. (2019) used Faster Region-based CNN (Faster R-CNN) to delimit the candidate regions of hyperbolic signals, and then adopted the so-called “double cluster seeking estimate” and “column-based transverse filter points” algorithms to further segment and fit the hyperbolic signals. Their method is proved to have ability of extracting useful features from synthetic and on-site GPR data sets. Liu et al. (2020) utilized Single Shot Multi-Box Detector (SSD) to recognize hyperbolic signals from GPR data for the cover thickness estimation, and the testing results showed that SSD outperforms Faster R-CNN in GPR hyperbolic signal recognition. Giannakis et al. (2020) combined neural network and random forest regression algorithm to estimate the diameter of reinforcement bars. Although their network was trained using entirely synthetic data, nonetheless, it performed sufficiently well using real data, showing good generalization capabilities.

The methods mentioned above applied deep learning to the GPR data processing and interpretation in NDT. To date, deep learning has not been applied to the interpretation of the fused data collected by multiple sensing techniques in NDT. Inspired by the previous work, this study combines deep learning algorithms with the processing and interpretation of EMI and GPR data, extending the potential applications of deep learning to the non-destructive evaluation of structural concrete. The proposed method takes full advantage of the information contained in different types of measurement data, aiming for autonomous and accurate evaluation of the cover thickness and reinforcement bar diameter. A deep learning algorithm, You Only Look Once-version 3 (YOLO v3), is deployed to locate and identify the hyperbolic signals from the radargrams, and the recognition performance is compared with the SSD method. The extracted hyperbolic signals, reflected from the reinforcement bars, are used for the rough estimation of the cover thickness range. Subsequently, the EMI data, accompanied with the roughly estimated cover thickness range, are imported to a one-dimensional CNN (1D CNN), which is pretrained by the calibrated EMI and GPR data collected from the in-house sand pit experiment, for autonomic estimation of the cover thickness and the diameter of reinforcement bars.

## 2 | METHODOLOGY

The proposed framework applies deep learning algorithms to EMI and GPR data for autonomic evaluation of the cover thickness and diameter of reinforcement bars in concrete. Figure 1 shows the flowchart of the data processing and interpretation combined with YOLO v3 and 1D CNN. In this frame, YOLO v3 is first trained by GPR data measured from two construction sites, and the trained

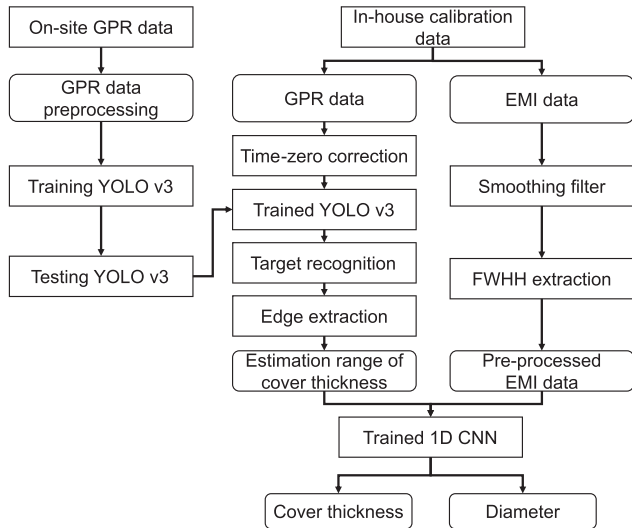


FIGURE 1 Flowchart of the reinforcement bar detection and evaluation

network is used to identify hyperbolic signals, which are reflected from the reinforcement bars. The use of YOLO v3 is to autonomously process large amounts of field GPR data in order to dramatically decrease the labor costs and time. Subsequently, Sobel operator, a frequently used edge extraction algorithm, is implemented to further extract the reflected signals from the identified regions. These extracted signals are deemed the real reflected wavelets from the bar surfaces. Then, by empirically evaluating the EM wave velocity in the background material, the cover thickness is roughly estimated and the possible range is constrained. The range values, as the prior information, are to be used for the subsequential reinforcement bar estimation. Another deep learning network—1D CNN—is introduced to simultaneously estimate the reinforcement bar diameter and cover thickness by fusing GPR and EMI data. The network is trained in advance with the calibration data measured in an in-house sand pit setup. The collected EMI data are preprocessed by smoothing filter, and an effective portion of EMI curves are extracted based on the principle of twice of FWHH. Finally, both the extracted EMI data and the estimated cover thickness range are imported into the trained 1D CNN, and the estimated cover thickness and diameter of the reinforcement bars are exported. More specific workflow and procedure of the proposed method are to be described in the following subsections.

It is noted that the current study is limited in the circumstances of single layer of reinforcement bars. Some special scenarios, for example, closely adjacent or welded steel bars, are not considered. In these complicated environments, the EMI signals are severely disturbed by the adjacent or additive metal components. In addition to the diameter of the reinforcement bars and the cover thick-

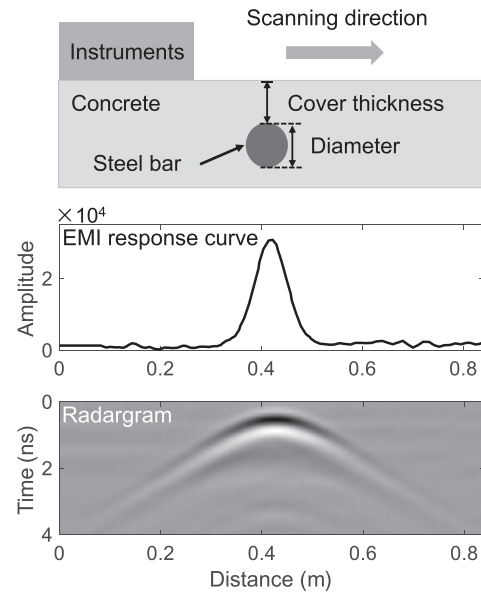


FIGURE 2 Schematic diagram of the in-house EMI and GPR calibration data acquisition. Note that the cover thickness in this study refers to the clear cover thickness, i.e., the distance between the concrete surface (or the sand surface in this setup) to the nearest surface of the reinforcement bars (Vélez et al., 2016)

ness, more variables are introduced to dominate the amplitudes and distribution characters of the EMI signals (Forde et al., 2013). Therefore, the estimation process becomes more sophisticated, and more prior information is needed to relieve the uncertainty and nonuniqueness.

## 2.1 | Data sets

Two types of data sets were collected for training the deep learning networks. One is the EMI data for 1D CNN training. They were measured in an in-house sand pit setup, and the data were calibrated with the configured cover thickness and diameter of the steel bars. The other is the GPR data for YOLO v3 training. They were measured in the realistic construction buildings, where a variety of typical reinforcement configurations are presented.

### 2.1.1 | In-house calibration data

The 1D CNN needs to be trained with the calibration data before it is used for the estimation of the bar diameter and cover thickness. To this end, it is critical to collect the EMI responses on the reinforcement bars with varying cover thickness and diameter. Figure 2 shows the schematic diagram of the in-house calibration data collection. The cover meter and GPR were slowly and uniformly moved upon the sand surface to collect the EMI responses and

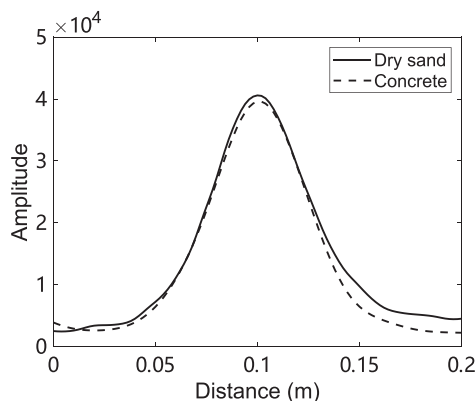


FIGURE 3 The EMI response curves measured in the backgrounds of dry sand and concrete, respectively

radargrams on the buried steel bars, where the survey lines are orthogonal to the axis of steel bars. The data directly collected on the construction sites are not applicable for training 1D CNN, because it is impossible to calibrate the measurement data with the true cover thickness and diameter of reinforcement bars unless massive destructive drillings are allowed.

Some researchers made use of gelatin or sand replacing concrete to carry out in-house reinforced concrete experiments (Warren & Giannopoulos, 2011; Wiwatrojanagul et al., 2017). In order to further verify the feasibility of substituting the concrete with some other materials in the current calibration work, a comparative experiment was carried out to study the influence of background materials on EMI response. A steel bar was, respectively, embedded in dry sand and concrete at a same depth, and EMI responses were collected. As Figure 3 shows, there are not observable differences in the EMI curves between dry sand and concrete. That is because their magnetic permeability and conductivity are extremely small relative to those of steel bar.

A sand pit setup was established to conduct the calibration experiment sand pit, as Figure 4 shows. The sand pit is filled with compacted dry sand to mimic the concrete material. A customized mechanical scanning frame was installed on the sand pit and can implement a three-dimensional motion in a stepping precision of 1 mm. A plastic plate with a thickness of 5 mm was linked with the mechanical arm of the scanning frame to lift the testing instruments. During the calibration measurements, a single reinforcement bar is horizontally buried inside the sand. By controlling the scanning frame, the plastic plate clears up the sand surface in a stepping mode, and thus can control the cover thickness with a precision of 1 mm. The previously mentioned dual-sensing prototype was utilized in this experiment to collect the EMI data (F. Zhou et al., 2018). The current excitation frequency is 40 kHz, and the EMI response is sensitive to a metal objective at a depth

TABLE 1 True reinforcement bar diameter and evaluated range of cover thickness corresponding to the retained EMI curves

Diameter (mm)	Range of cover thickness (mm)
6	[5, 20]
8	[5, 27]
10	[5, 38]
12	[5, 51]
14	[5, 54]
16	[5, 59]
18	[5, 60]
20	[5, 60]
22	[5, 60]
25	[5, 60]
28	[5, 60]

up to 100 mm (Gao et al., 2015). A commercial GPR system with a center frequency of 2.6 GHz was used for GPR data collection. It is a ground-coupled radar system with a pair of bowtie antennas. In general concrete materials, the penetrating depth can reach 500 mm (Liu et al., 2021).

Eleven round steel bars with different diameters were used as samples for the calibration experiments, referring to the Chinese Industrial Building Standards (Zhu et al., 2017). The diameter of the steel bars is 6, 8, 10, 12, 14, 16, 18, 20, 22, 25, and 28 mm, respectively. The cover thickness was decreased from 60 mm to 5 mm with a stepped interval of 1 mm. Therefore, there are a total of 616 configuration schemes of steel bars. Considering the systematic errors caused by the intrinsic noise of the used dual-sensing prototype, for each configuration scheme of the reinforcement bars, measurements were taken for six times, with a total of 3696 sets of EMI data collected. Figure 5 presents some typical EMI curves collected in the sand pit. The data were processed by smoothing to alleviate the measuring errors and noise effects. In addition, in some cases that the reinforcement bar diameter is excessively small while the cover thickness is excessively large, the EMI intensity becomes comparable with the noise, and therefore the target responses are difficult to be distinguished, as Figure 6 shows. For this reason, some data sets without recognizable target signals were ticked out of the training data set. As a result, a total of 1898 sets of EMI data were retained for the following processing and interpretation. Table 1 shows the setting range of the cover thickness and diameter corresponding to the retained EMI data. Generally, in the EMI curves, the portions above the half of the peak value, defined as FWHH, are extracted as the effective signals for the reinforcement bar estimation (Quek et al., 2003; Zaid et al., 2004). To further utilize the information contained in the EMI curves, the signals above the twice of the width at

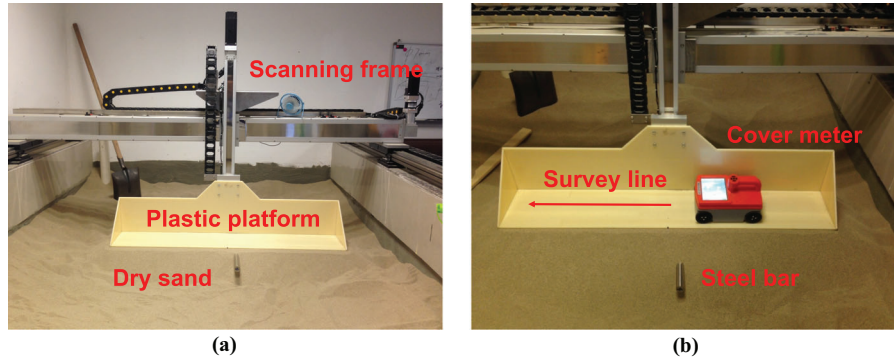


FIGURE 4 Photos of in-house calibration setup: (a) three-dimensional movable scanning frame and (b) measurement scheme

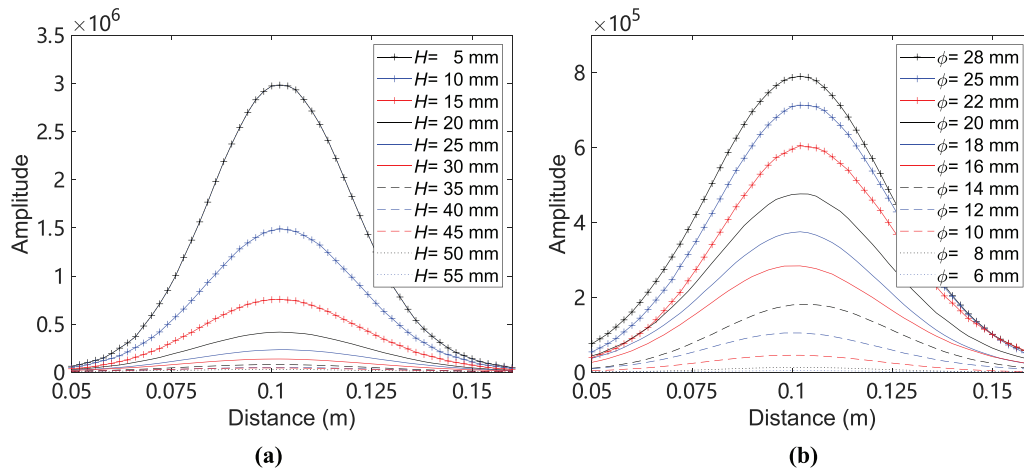


FIGURE 5 Samples of EMI curves (a) when reinforcement bar diameter is 20 mm for different cover thickness ( $H$ ) and (b) when the cover thickness is 20 mm for different diameter ( $\phi$ )

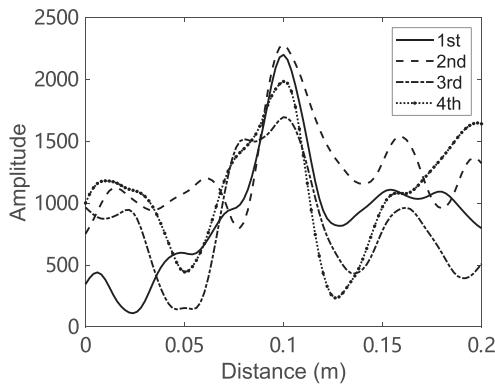


FIGURE 6 EMI curves submerged by noises when the reinforcement bar diameter is 6 mm and the cover thickness is 30 mm

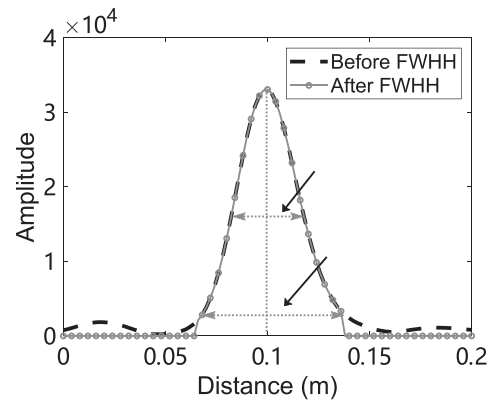


FIGURE 7 Extracting the effective EMI with twice of FWHH. The symbol  $2W$  represents twice of FWHH, i.e., the extracted EMI segment corresponding with twice of the width at the half height of the peak

the half height of the peak were extracted as the imported data of the 1D CNN, as illustrated in Figure 7.

In the in-house EMI measurements, there exist certain cases that the steel bars generate highly similar EMI

response curves in different settings. Figure 8 presents a typical example measured in the setup. This finding, in turn, proves that a single EMI sensing technique tends to

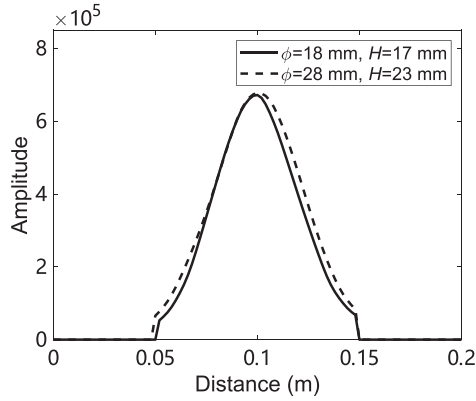


FIGURE 8 Example of similar EMI curves with different reinforcement bar settings

derive multiple solutions, which has been widely acknowledged by the NDT community (Quek et al., 2003). In the practical applications, one solution is to preset either the cover thickness or the reinforcement bar diameter (Forde et al., 2013); and the other is to collect extra information as a constraint condition for accurately inferring, exemplified by the dual orthogonal EMI sensing method (Allred, 1995). In this study, GPR data were collected accompanied with EMI measurements, and the possible range of the cover thickness was roughly evaluated using the GPR data as the constraint condition for EMI estimation.

Figure 9 shows the workflow of GPR data processing in this study. First, time-zero correction was conducted to pick up the starting point of EM wave propagation on the sand surface. Next, the hyperbolic signals were identified and extracted with a well-trained YOLO v3 network. Then, the direct wave was removed to retain only the reflected signals. Some regular denoising approaches, such as wavelet threshold denoising and median filtering, were conducted to improve the quality of the radargrams (Jol, 2008). Afterwards, an edge extraction algorithm, Sobel operator, was adopted to extract the edge curves of the hyperbolic signals (Sami & Abdulmunem, 2020). Subsequently, the coordinates of the vertex of the hyperbolic signal were determined. By this means, the two-way travel time, that is, the time taken for an EM wave to propagate from the transmitter down to a reflector and back to the receiver, is acquired. Finally, with the actual spacing between the transmitting and receiving antennas and the evaluated wave velocity, the cover thickness is roughly derived by the formulas below:

$$H = \frac{1}{2} \sqrt{S^2 - x^2} \quad (1)$$

$$S = vt \quad (2)$$

$$v = \frac{c}{\sqrt{\epsilon_r}} \quad (3)$$

where  $H$  is the cover thickness,  $S$  is the actual travel distance of EM wave,  $x$  is the antenna spacing,  $v$  is the EM wave velocity in the background material,  $t$  is the two-way travel time,  $c$  is the EM wave velocity in free space, that is, 0.3 m/ns, and  $\epsilon_r$  is the relative permittivity of the background material. In the sand pit experiment, the relative permittivity of dry sand was assumed to range from 3 to 5. Time-depth conversion was implemented to derive the cover thickness through the measured travel time and the evaluated wave velocity.

### 2.1.2 | On-site GPR data

A great number of radargrams, which represent realistic and diverse reinforced concrete scenarios, are required to train a YOLO v3 network. The GPR data used in the identification of hyperbolic signals were collected from two newly completed residential buildings located in Guangzhou, China. The commercial GPR system was operated on the concrete wall sides to collect the radargrams, which contain reflected signals from the reinforcement bars. The majority of data were collected on the slabs where a single layer of reinforcement bars are embedded inside, whereas a small portion of data were from the beams and columns with multiple layers of steel bars. Normally, the slabs account for the large percentage of the reinforced concrete constructions in a residential building. Therefore, most GPR data contain signals reflected from a single layer of reinforcement bars, which substantially simplifies certain complicated scenarios but accords with the investigation scope of this study as specified before.

The measured reinforcement bars have diverse diameter, cover thickness, and spatial distribution. The diameter changes between 6 and 25 mm, the cover thickness changes between 5 and 30 mm, and the spaced distance changes between 40 and 300 mm. Note that the basic information of reinforcement bar settings were obtained by referring to the construction drawings. Certain deviations, which exist in the practical constructions, do not have an essential impact on the network training and verifying because the use of YOLO v3 aims only for automatically extracting the hyperbolic signals instead of quantitatively evaluating the reinforcement bars.

Due to the GPR polarization effects (Slob et al., 2010), the measurement lines were taken perpendicular with the direction of the reinforcement bars to collect the strong reflected signals from the steel bars. The measurements

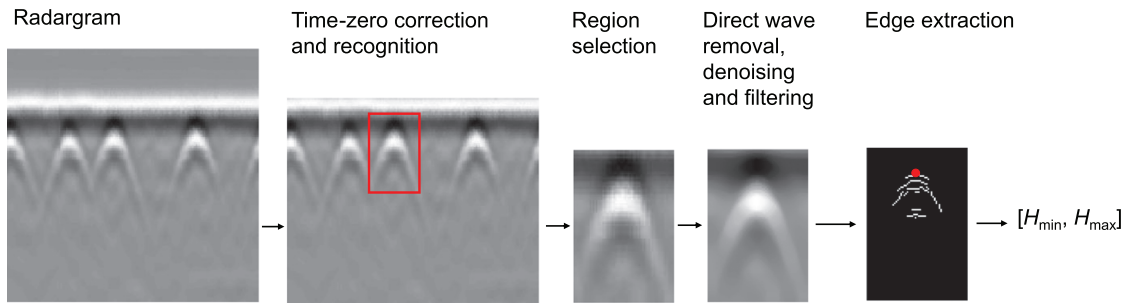


FIGURE 9 Flowchart of processing GPR data

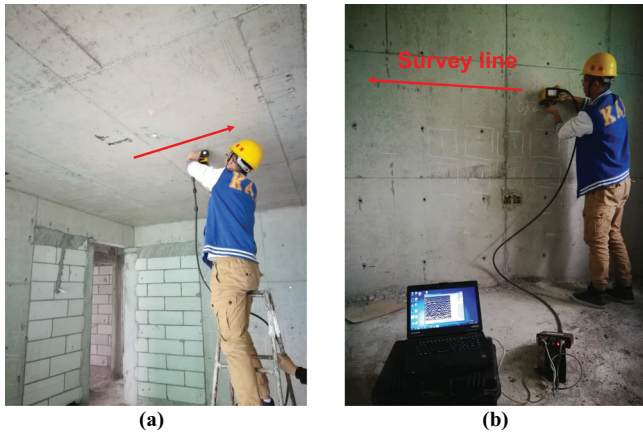


FIGURE 10 Photos of the on-site data acquisition from (a) ceilings and (b) walls

were kept away from the binding points to avoid the interference from the additional metal components. Totally, 9143 hyperbolic signals were obtained from the radargrams collected in the construction buildings. These radargrams are to be utilized to train the YOLO v3 network for hyperbolic signal identification. Figure 10 shows the on-site data collection, and Figure 11 demonstrates several typical radargram samples.

## 2.2 | Network architectures

### 2.2.1 | YOLO v3

In this study, a deep learning architecture of YOLO v3 is used to recognize hyperbolic signals in the radargrams because it outperforms some other networks by balancing recognition accuracy and speed (Redmon & Farhadi, 2018). Figure 12 shows the architecture of YOLO v3, which is a fully convolutional network primarily connected by a series of residual (Res) layers and convolutional (Conv) layers. Taken as a whole, the architecture of YOLO v3 contains a backbone network called Darknet-53 (Figure 12(a)), which is responsible for extracting the convolutional fea-

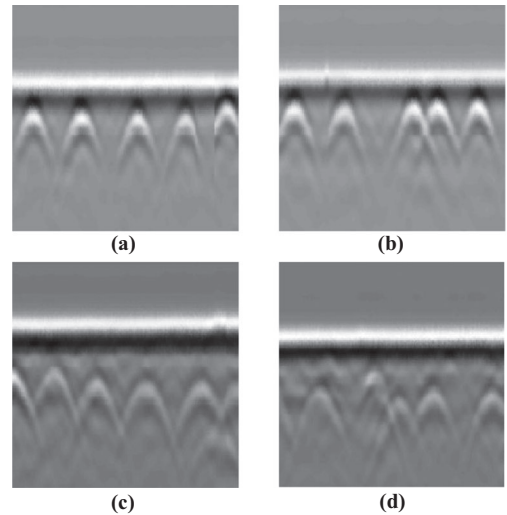
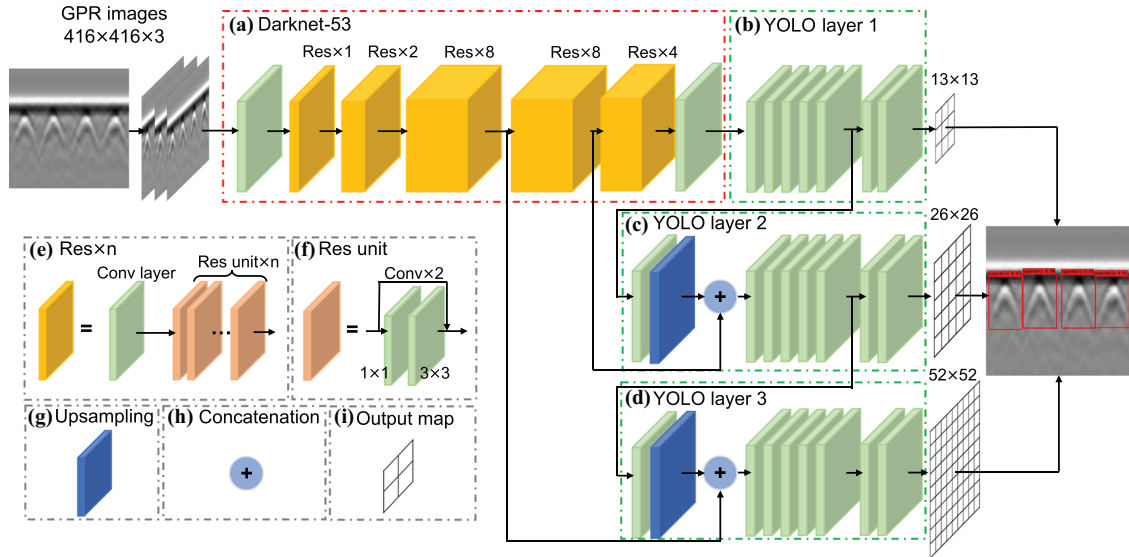


FIGURE 11 Hyperbolic signals in GPR data samples collected from (a) evenly distributed and (b) (c) (d) densely distributed reinforcement bars

ture maps of the input images (Krizhevsky et al., 2017). This part consists of two Conv layers and five Res modules (Figure 12(a)). The five Res modules are composed of a Conv layer and Res units of 1, 2, 8, 8, and 4, respectively (Figure 12(e)). Each Res unit consists of a 1x1 and 3x3 Conv layer (Figure 12(f)). The total number of Conv layers in this part is 53. The Conv layers implement three sequential operations—convolution, batch normalization, and leaky rectification linear unit activation. In Darknet-53, the considerable number of the Conv layers can greatly improve the performance of the network. In principle, the deeper the neural network is, the more powerful the capability of image identification is. However, an excessively deep network is prone to a vanishing gradient problem, and thus lowers the network performance (Bengio & LeCun, 2007). To solve this problem, in each Res units, the input is added to the output (Figure 12(f)) to retain the influence of the previous Res units. In addition, a Conv layer with a stride of 2 is inserted in the front of each Res module (Figure 12(e)) to implement downsampling, which reduces half of the dimensionality (width and height) of the feature maps.



**FIGURE 12** Network architecture of YOLO v3 for GPR hyperbolic signal identifications. The basic network units are Conv layers (green blocks). The network structure is divided into two parts: (a) backbone network composed of Darknet-53, and (b)–(d) YOLO layers composed of only Conv layers or Conv layers concatenated by upsampling layers. The other functional units include: (e) Res module (yellow) consisting of a Conv layer and several Res units, (f) Res unit (brown) consisting of two Conv layers, (g) upsampling layer (blue), (h) concatenation operator, and (i) output map

After extracted by Darknet-53, the feature maps, representing three different scales, are, respectively, imported to three sets of standard Conv networks (Figures 12(b)–(d)) for constructing multiple-scale feature maps. The feature maps, which undergo more Conv operations (Figure 12(b)), have lower resolutions, smaller scales, and less information, and are suitable only for detecting larger scale targets in the images. To recognize targets with smaller scales, the feature maps with smaller scale are upsampled and then concatenated with the larger scale feature maps, which are obtained by less Conv operations (Figures 12(c) and (d)). The resulting feature maps contain more information and can recognize targets with smaller scales at higher resolutions. In this study, three different scales of feature maps are used to detect targets with the sizes of  $13 \times 13$ ,  $26 \times 26$ , and  $52 \times 52$  pixels, respectively, and the identified targets are marked with a bounding box and an indicator of confidence. More details on YOLO v3 architecture can be found in Redmon et al. (2018).

### 2.2.2 | 1D CNN

The effective EMI curves extracted with FWHH method and the ranges of the cover thickness, which are estimated from GPR data, are treated as 1D vectors. Therefore, a 1D CNN is designed referring to the Visual Geometry Group-16 network architecture, which is typically used in image recognition (Simonyan & Zisserman, 2014).

Figure 13 shows the architecture of the 1D CNN. There are four Conv blocks, and each Conv layer sequentially performs convolution, batch normalization, and rectified linear unit activation. The established 1D CNN is primarily composed of a number of 1D Conv layers. Following each Conv block, a max pooling layer is deployed to reduce the dimensionality of features. Finally, four fully connected layers are used to output the predicted values, among which the first three layers apply L2 regularization to reduce overfitting (Cortes et al., 2012). In addition, a global average pooling layer is inserted between the Conv blocks and the fully connected layers to reduce the number of parameters and mitigate overfitting (Lin et al., 2013). The 1D vectors containing the effective EMI curve and the cover thickness range are imported into the 1D CNN as the input variables, while the cover thickness and reinforcement bar diameter are the estimated values exported from the output nodes.

## 3 | RESULTS

Training and testing the YOLO v3 network were performed on the Google Colaboratory, a cloud platform deployed with the deep learning environments. In terms of the evaluation of the cover thickness and diameter of reinforcement bars, the training and testing were run on a personal computer with Intel I7-9750H CPU and RTX 2070 8G GPU. The open source software compilation library TensorFlow 2.0 was used for deployment.

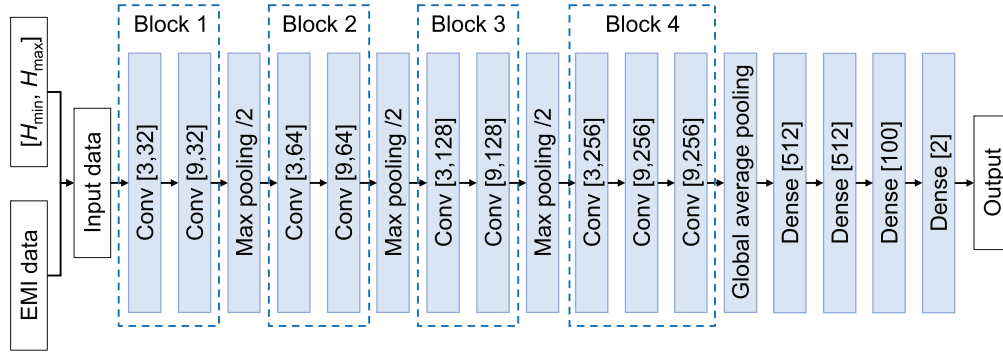


FIGURE 13 Network architecture of 1D CNN for evaluation of cover thickness and diameter of reinforcement bars

### 3.1 | Hyperbolic signal identification

To match the size of the input unit of YOLO v3 network, the continuously measured radargram, which contains a total number of 9143 hyperbolic signals, was divided into 1877 images with a size of 416×416 pixels. All the images were randomly divided into training set (80%) and testing set (20%). In the training set, 20% of the training data were used as the validation set to verify the generalization of the network during the training (Chollet, 2017). After training, the testing set was used to evaluate the performance of YOLO v3. The YOLO loss, a key indicator of YOLO v3, was adopted as the loss function. To improve performance of the YOLO v3 network, transfer learning, which migrates the pretrained model to the new model, was adapted in the network training process (Yosinski et al., 2014). Therefore, the pretraining weights of Darknet-53, which was well trained with the ImageNet data set, were loaded to initialize the weights of network (Krizhevsky et al., 2017). Initially, the learning rate was set to  $10^{-3}$ , and subsequently, it was set to  $10^{-4}$  and  $10^{-5}$  at the 1600th and 1800th iterations, respectively, using a momentum of 0.9 and a weight decay of  $5 \times 10^{-4}$ . The batch size and subdivisions were set to 64 and 8, respectively, to maximize the utilization of GPU memory. To enhance the robustness of the network, random multiscale training and data augmentation were applied during the training process. Random multiscale training was used to generate new images with different resolutions (Redmon & Farhadi, 2018). The image resolutions at each iteration were randomly set in the range from 320×320 to 608×608 pixels with a stride of 32 pixels. Data augmentation was used to generate more data based on the existing data to increase the number of the samples by randomly changing the saturation, exposure, and hue of the training data (Wong et al., 2016). The confidence threshold, ranging between 0 and 1, was set to 0.3.

Figure 14 displays some correctly recognized reinforcement bars by the YOLO v3 network in diverse reinforced

structures. The detected reinforcement bars were framed with red bounding boxes. Meanwhile, each bounding box was labeled with the category name (i.e., “hyperbola”) and a confidence value above the confidence threshold of 0.3. The confidence reflects how the model ensures that the box contains a hyperbolic signal reflected by a reinforcement bar (Redmon et al., 2016). From Figures 14(a)–(e), it can be seen that all of the hyperbolic signals reflected by the reinforcement bars were successfully identified, including some complicated scenarios. In particular, Figures 14(d)–(f) show that even if the reinforcement bars are in dense and staggered distributions and the reflected signals are blurred and overlapped, YOLO v3 has the capability of identifying these hyperbolic signals with a high confidence.

In order to evaluate the performance of YOLO v3 in identifying hyperbolic signals, three indicators, that is, precision ( $Pr$ ), recall ( $Re$ ), and  $F$ -score, were introduced as formulated by:

$$Pr = \frac{TP}{TP + FP} \quad (4)$$

$$Re = \frac{TP}{TP + FN} \quad (5)$$

$$F\text{-score} = \frac{2Pr \cdot Re}{Pr + Re} \quad (6)$$

where  $TP$  stands for the True Positive,  $FP$  for the False Positive, and  $FN$  for the False Negative. Table 2 shows an overview of the evaluation metrics on hyperbolic signal identification. True Positive is the number of correctly identified hyperbolic signals. False Positive is the number of the signals that are misidentified as hyperbolic signals, which are caused by clutter or noise. False Negative is the number of hyperbolic signals that are unrecognized. True

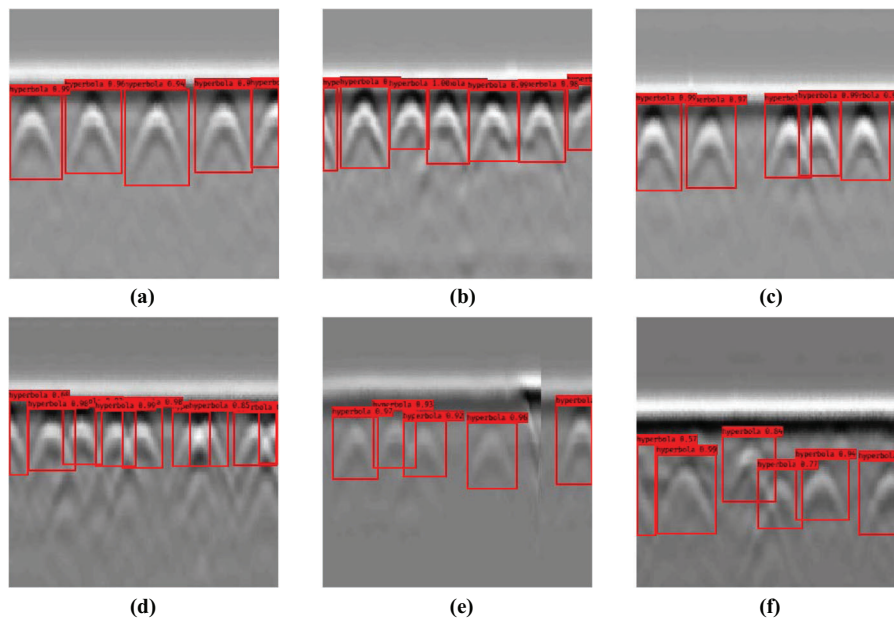


**FIGURE 14** Identified hyperbolic signals with YOLO v3 when the reinforcement bars are (a) evenly distributed, (b) closely distributed, and (c) unevenly distributed, and when the reflected signals are (d) excessively overlapped, (e) blurred, and (f) blurred and overlapped

**TABLE 2** Evaluation metrics of hyperbolic signal identification

Predicted	Ground truth	
	Hyperbolic signal	Background
Hyperbolic signal	True Positive	False Positive
Background	False Negative	True Negative

Negative is the number of the background signals that are not identified as hyperbolic signals, which is not included in Equations (4)–(6). In this study, precision expresses the number percentage of the correctly identified hyperbolic signals out of the total signals classified into the hyperbolic signals, and recall is the number percentage of the correctly identified hyperbolic signals out of all the true hyperbolic signals.

In fact, precision and recall are two incompatible indicators. Increasing the precision tends to cause some of the hyperbolic signals misrecognized, resulting in a decreased recall; conversely, increasing the recall tends to cause some of the background signals to be identified as hyperbolic signals, resulting in a decreased precision. Therefore, it is not practical to simultaneously keep both of the indicators at a high level. For this reason, *F*-score is introduced to evaluate the performance of the network since it is the harmonic mean of the precision and recall, as formulated in Equation (6). In addition, frame per second (FPS), which reflects the number of the frames that are processed in a unit time, is introduced to evaluate the processing speed of the network.

Some other target identification algorithms have been applied to hyperbolic signal recognition in the radargrams,

**TABLE 3** Performance comparison of hyperbolic signal identification with SSD and YOLO v3 methods

Method	Precision (%)	Recall (%)	<i>F</i> -score (%)	FPS
SSD	92.77	76.61	83.92	9.09
YOLO v3	94.62	95.28	94.45	9.97

of which SSD has proved to be superior to conventional processing algorithms exemplified by Faster R-CNN (Liu et al., 2020). To evaluate the performance of YOLO v3 in hyperbolic signal recognition, the same data set was used to train and test the SSD network, and the results of the two algorithms were compared with the aforementioned indicators. As Table 3 shows, the precision of YOLO v3 is 94.62%, the recall is 95.28%, and the *F*-score is 94.45%, which are higher than those of SSD. In particular, the recall and *F*-score of YOLO v3 are significantly higher than those of SSD, implying that YOLO v3 can recognize a greater number of hyperbolic signals at a higher accuracy than SSD. In terms of processing speed, both networks can process approximately nine images per second, and the FPS of YOLO v3 is slightly higher than that of SSD. In practice, the movement speed of the instrument is limited under the radargram processing speed to ensure the synchronization of the on-site data collecting and processing. The current processing speed of YOLO v3 and SSD can satisfy a real-time reinforcement bar identification.

The precision–recall (P-R) curve and receiver operating characteristic (ROC) curve are introduced as the comprehensive evaluation indicators (Bradley, 1997; Chinchor & Sundheim, 1993). The cumulative areas under the

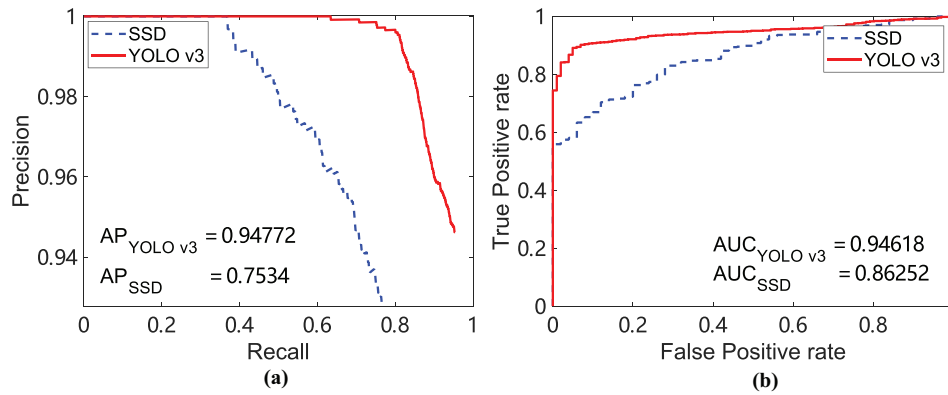


FIGURE 15 Comparison of the performance of SSD and YOLO v3 by (a) P-R curve and (b) ROC curve

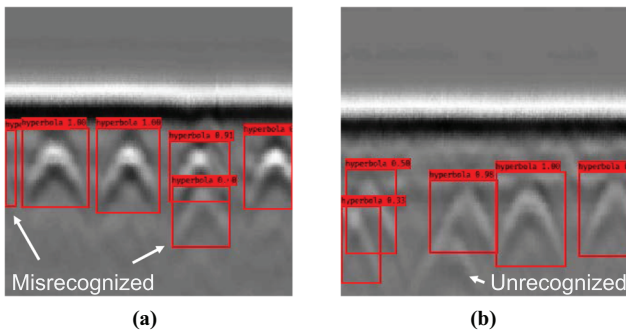


FIGURE 16 Cases that hyperbolic signals are (a) misrecognized and (b) unrecognized by YOLO v3

P-R curves are called average precision (AP), representing the performance of the network on recognizing the True Positives. The area under the ROC curve (AUC) signifies the probability that the network ranks a random positive example more highly than a random negative example. These two areas range value from 0 to 1, which can explicitly compare the performance of different networks, where a larger area implies a higher network performance. In the reinforcement bar recognition, hyperbolic signals are treated as positive samples, whereas the background signals are treated as negative samples. When the ratio of positive to negative samples is large, the P-R curve can better reflect the recognition performance. When the positive and negative samples have similar numbers, the ROC curve has a strong robustness since it takes both positive and negative samples into account. Figure 15 shows that the AP and AUC of YOLO v3 in this study are 94.8% and 94.6%, respectively, which are higher than those of SSD (75.4% for AP and 86.3% for AUC, respectively). The comparisons between the two plots evidently indicate that YOLO v3 outperforms SSD in hyperbolic signal identification of radargrams.

However, there still exist some cases that hyperbolic signals are misrecognized or unrecognized. Figure 16(a)

shows two misrecognition cases. In this image, four hyperbolic signals reflected by the reinforcement bars are correctly identified and labeled with bounding boxes; however, two pseudo target echo signals are wrongly identified as true hyperbolic signals. The misrecognition of the first pseudo target signal (on the left side of the image) is mainly caused by the image segmentation. A continuously measured radargram needs to be segmented into a series of small-size images for training. Some hyperbolic signals adjacent to the edge of the image are truncated and then labeled for training the network. These parts of signals have high similarity with the pseudo target signals, and therefore the trained network is prone to misrecognize the pseudo target signal as a truncated hyperbolic signal. The other misrecognized signal (in the lower part of the image) may be aroused by a nonmetallic buried object. For example, a gravel stone with the size comparable to a steel bar can generate a hyperbolic signal with the relatively weak amplitude. This signal is possibly recognized as a hyperbolic signal reflected by a reinforcement bar once they have some similarities on signal features.

Figure 16(b) shows an unrecognized case. There are six hyperbolic signals in the radargram, among which five are correctly identified and labeled with bounding boxes. However, at the left bottom of the image, a hyperbolic signal is not recognized although it is clearly visible. This is inferred to be caused by the relatively weak amplitude of the reflected signal. In addition, another possible cause is that portions of the hyperbolic signal are overlapped with the adjacent signal reflected from a steel bar. This inference can be further verified by the hyperbolic signal, which is located in the left bottom and overlapped by the upper one. This signal is correctly identified, but its confidence is as low as 0.33. The data from the complicated scenarios account for a relatively low portion of the data collected from the buildings, less than 10%. To decrease the rates of misrecognition and unrecognized, a practical

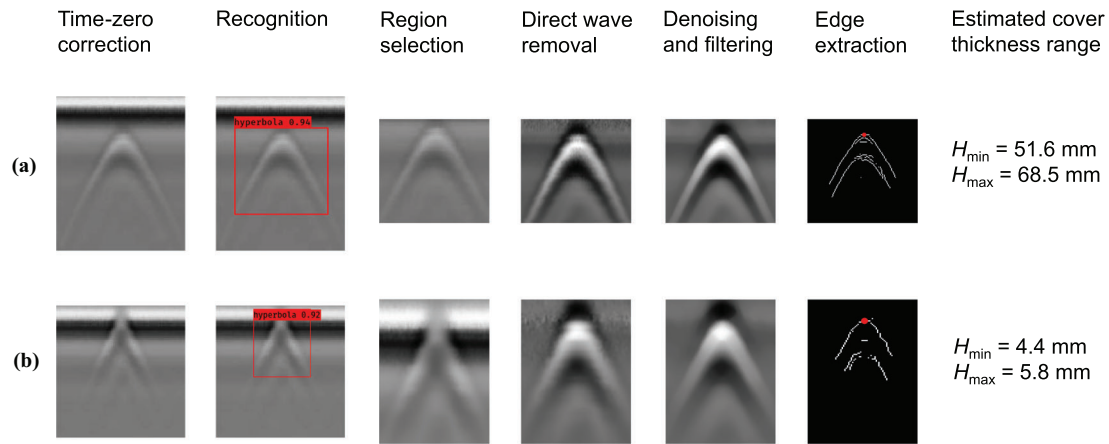


FIGURE 17 Examples of roughly estimated cover thickness range through radargrams when the true cover thickness is (a) 60 mm and (b) 5 mm, respectively

solution is to further increase the number of the training samples, which can represent more complicated and diverse scenarios.

The radargrams collected in the in-house calibration experiment are imported to the trained YOLO v3 for hyperbolic signal identification. All hyperbolic reflection signals are successfully identified. After data processing, the ranges of the cover thickness are roughly estimated and regarded as constraints for the accurate evaluation of cover thickness and reinforcement bar diameter. Figure 17 shows two sets of estimated cover thickness range when the true cover thickness is 60 mm and 5 mm, respectively.

### 3.2 | Reinforcement bar evaluation

The effective EMI curves, extracted with twice of FWHH, and the possible range of cover thickness, evaluated by GPR data, are concatenated into a 1D vector and imported into the 1D CNN. The estimated values of the cover thickness and diameter of reinforcement bars are exported from the network. Among the 1898 sets of EMI data, the number allocation of training sets, testing sets, and validation sets follow the proportions allocated in the YOLO v3 network, as stated in Section 3.1. After network training, 380 sets of EMI data were utilized to evaluate the performance of the 1D CNN. In the training process, the mean square error was selected as the loss function. The network employed the Adam optimizer to implement 5000 iterations with a batch size of 256 (Kingma & Ba, 2014). The initial learning rate was  $10^{-3}$  with a decay factor of 0.1 and a patience of 200. This signifies that if the validation loss does not decline after 200 iterations, the learning rate will reduce to one-tenth of its current value for the convergence of the network.

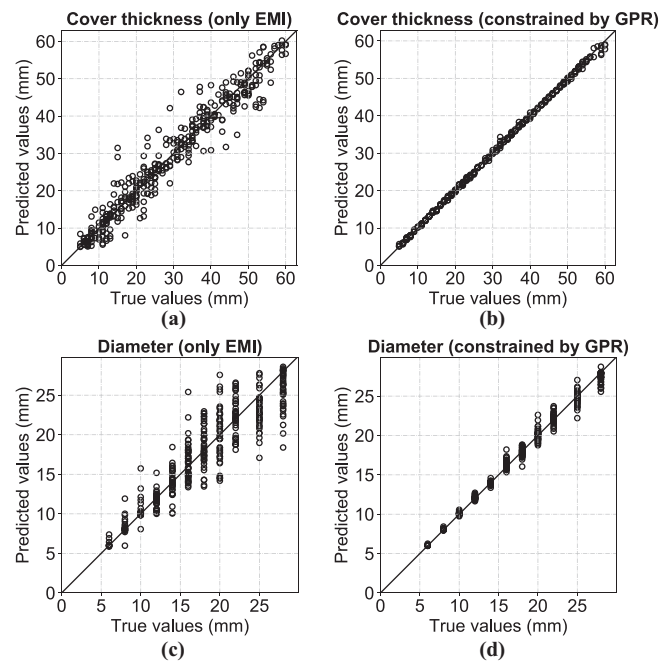
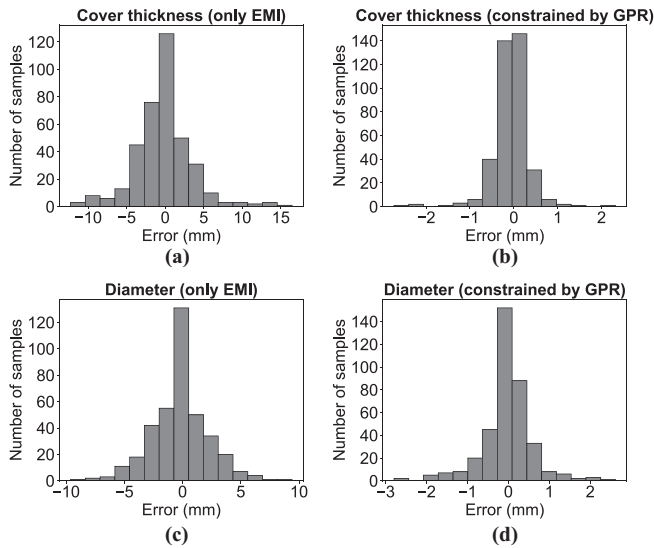


FIGURE 18 Comparisons of estimated results with scatter diagrams: (a) cover thickness estimated by 1D CNN without any constraint, (b) cover thickness estimated by 1D CNN under the constraint of the possible range of the cover thickness, (c) diameter of reinforcement bars estimated by 1D CNN without any constraint, and (d) diameter of reinforcement bars estimated by 1D CNN under the constraint of possible range of the cover thickness

In order to evaluate the performance of the combination of EMI and GPR data in improving the estimation accuracy, a network trained by the sole EMI data was tested, and the estimated results were compared with the current method. Figure 18 presents the estimated and true values of the cover thickness and reinforcement bar diameter obtained by the two different methods, and Figure 19 compares the statistical distributions of the estimation errors.



**FIGURE 19** Comparisons of estimated results with error bars: (a) cover thickness estimated by 1D CNN without any constraint, (b) cover thickness estimated by 1D CNN under the constraint of the possible range of the cover thickness, (c) diameter of reinforcement bars estimated by 1D CNN without any constraint, and (d) diameter of reinforcement bars estimated by 1D CNN under the constraint of possible range of the cover thickness

**TABLE 4** Accuracy with different permissible errors

Permissible error (mm)	Accuracy	
	Cover thickness (%)	Diameter (%)
1	96.8	90.3
2	98.9	98.2
3	100	100

It can be seen that in the sole EMI estimation, there exist considerable errors, up to 15 mm, between the estimated and true values (Figures 19(a) and (c)). On the contrary, in the combined EMI and GPR method, the estimation errors, both for cover thickness and diameter of reinforcement bars, are below 3 mm, and the majority of the tested samples have the estimation errors within 1 mm (Figures 19(b) and (d)). The comparisons imply that the method combining the cover thickness range as a constraint condition greatly decreases the estimation errors compared with the method using the sole EMI data. It is safely concluded that in the proposed estimation scheme, the range of the cover thickness, derived by GPR data, plays an essential role in improving the estimation accuracy.

In practical engineering applications, there exists an acceptable error range. Table 4 counts the accuracy of the proposed method when the permissible errors are 1, 2, and 3 mm, respectively. It can be seen that under a permissible error of 1 mm, over 90% of the reinforcement bars in the

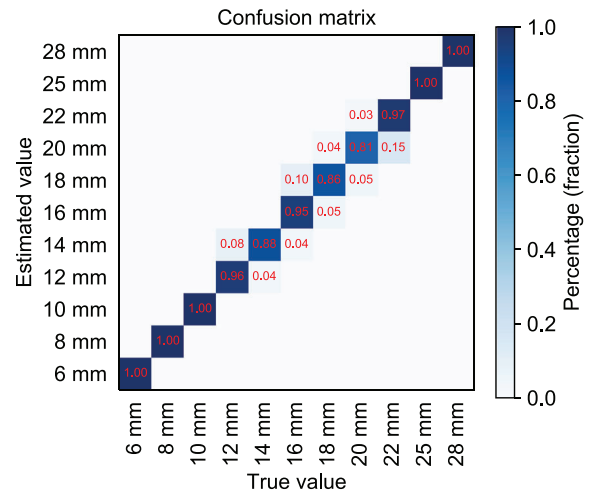


**FIGURE 20** Confusion matrix of estimated and true values of reinforcement bar diameter

experiment are accurately estimated; while once an error of 3 mm is acceptable, all the reinforcement bars are accurately estimated. The statistical results demonstrate that the estimation accuracy is sufficient for engineering applications.

In practical constructions, the used reinforcement bars have discrete values of diameter with the size intervals of 2, 3, or 5 mm according to the industrial standards (Zhu et al., 2017). Therefore, the initially predicted values of the reinforcement bar diameter are artificially classified to the nearest possible values. In this experiment, the samples of reinforcement bars have a diameter of 6, 8, 10, 12, 14, 16, 18, 20, 22, 25, and 28, with the size intervals of 2 and 3 mm, respectively. In this case, if the true diameter of the reinforcement bars is 10 mm while the initial prediction is 8.9 mm, then the estimated result is 8 mm instead of 9 mm, signifying an error of 2 mm. Similarly, if the reinforcement bar with a true diameter of 22 mm is initially predicted as 25.5 mm, then the estimated diameter is 25 mm, which means the estimation error is 3 mm. A confusion matrix was introduced to assess the deviation between the estimated and true values in the reinforcement bar diameter, as Figure 20 presents. In the diagram, the reinforcement bars with the same diameter are treated as an independent sample category, wherefore there are totally 11 categories. It can be seen that when the diameter of the reinforcement bars is smaller than 12 mm or larger than 22 mm, the estimated values agree with the true values; whereas when the diameter ranges from 12 to 22 mm, the numbers of the accurately estimated samples account for 81% to 97% of the tested sample numbers in the respective categories. These inaccurately estimated samples are classified to their nearest categories.

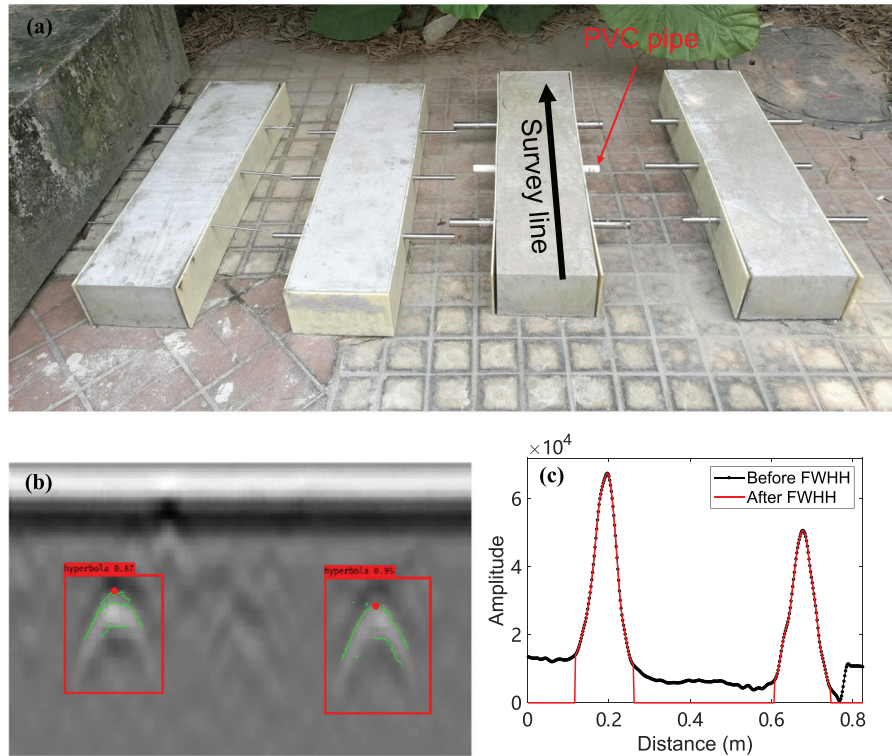


**FIGURE 21** Specimen experiment photo and acquired data: (a) four casted concrete specimens embedded with 11 round steel bars and one PVC pipe, (b) GPR radargram after hyperbolic signal recognition and edge extraction, and (c) EMI data before and after FWHH processing

### 3.3 | Verification with specimens

In the concrete environment, the EMI responses are highly similar with those in the sand (as explained in Section 2.1.1); while the GPR data have certain differences as the permittivity of sand differs from that of concrete. In this proposed method, GPR data are treated solely as a constraint condition through roughly evaluating the possible range of the cover thickness. Therefore, even though the 1D CNN is trained by sand pit data, it can be adapted in the realistic concrete structures after repredicting the concrete permittivity.

To further verify the proposed method, an outdoor specimen experiment was conducted. Four concrete specimens were casted and cured in the outdoor environment following the industrial criterions, as Figure 21(a) shows. A total of 11 round steel bars were embedded in the specimens with their diameter ranging from 6 to 28 mm and cover thickness ranging from 15 to 50 mm. An additional polyvinyl chloride (PVC) pipe was embedded in one of the specimens to test the identification ability of the YOLO v3 network for the pseudo target signals. The dimensions of the concrete specimens are  $1000 \times 250 \times 150 \text{ mm}^3$ . The instruments were operated along the survey line on the

specimens, collecting GPR and EMI data. Figures 21(b) and (c) show the preprocessed radargram and EMI curve, which were collected on the concrete specimen containing the PVC pipe. It can be seen that two target signals reflected from the steel bars were successfully identified and extracted by the YOLO v3 network and edge extraction algorithms. The PVC pipe arouses weak reflected waves relative to the steel bars, and therefore its echo was not recognized. In the meanwhile, the PVC pipe contains no metal and therefore contributes nothing to EMI responses.

The EMI and GPR data collected from the specimens were tested using the well-trained 1D CNN as described early. The relative permittivity in the concrete was roughly set from 6 to 11 (Forde et al., 2013). Referring to the instruction of commercial cover meters and industrial technical standards on reinforcement bar testing, the permissible error was set as 1 mm in this experiment (Zhang et al., 2019). Table 5 shows that among the 22 estimated values, there are 17 values correctly estimated, while the 5 inaccurately estimated values have errors of 1 mm or 2 mm. The testing results from the specimen experiment further verify the effectiveness and accuracy of the proposed non-destructive estimation method in the reinforced concrete structures.



**TABLE 5** The estimation results of cover thickness and diameter of the reinforcement bars by 1D CNN with a permissible error of 1 mm

Cover thickness			Diameter		
True (mm)	Estimated (mm)	Error (mm)	True (mm)	Estimated (mm)	Error (mm)
15	15	0	6	6	0
21	21	0	8	8	0
25	25	0	10	10	0
37	37	0	12	12	0
35	35	0	14	14	0
42	42	0	16	18	2
32	34	2	18	18	0
38	39	1	20	20	0
43	43	0	22	20	-2
46	48	2	25	25	0
50	50	0	28	28	0

## 4 | DISCUSSION

The results from the experiments with in-house sand pit and concrete specimens indicate that the proposed method can autonomously and accurately evaluate the diameter of reinforcement bar and cover thickness. The deep learning algorithm YOLO v3, which has been widely applied to the general target identification in the image processing field, is verified to have the capability of recognizing echo signals in GPR images. The successful application is based on the principle that a mass of hyperbolic signals are treated as typical image features to train the YOLO v3 network. As previously mentioned, the sole EMI data tend to bring about multiple solutions when inferring the reinforcement bar diameter and cover thickness. The introduction of GPR data can provide extra information to characterize the position features of the reinforcement bars. The cover thickness derived by GPR data, in spite of a rough range, can impose an essential constraint on the interpretation of EMI data, wherefore relieves the multiple solutions and improves estimation accuracy. The 1D CNN, primarily consisting of multiple Conv layers, can fuse GPR and EMI data, and autonomously map the features of EM signals with the cover thickness and the diameter of the reinforcement bars.

In the experiments of hyperbolic signal identification, there are still few reflected signals unrecognized or misrecognized in certain complicated scenarios. The phenomena are due to the fact that the samples in the training set do not represent all realistic possibilities. In principle, increasing the sample amount of field data in different scenarios can further improve the performance of the network (Chen & Lin, 2014). However, it costs more human resources, and some special scenarios are not often encountered in the realistic environments. When estimating the cover thickness and diameter of reinforcement bars with 1D CNN,

the estimation errors are primarily produced from two aspects: (1) the noise arising from the instrument system and the external environments and (2) the deviation of the roughly estimated wave velocity from its true value. The former mainly makes influence on the EMI responses, whereas the latter on the GPR estimated cover thickness range. To relieve the noise effects, a practical solution is to make multiple measurements on the same reinforcement bars, as have been conducted in the sand pit experiments. The errors brought by the roughly estimated wave velocity range can be decreased if a narrow velocity range is imposed. However, the following problem is that the robustness of the network will decline.

In the realistic reinforced concrete structures, round steel bars and ribbed steel bars are two types of frequently used reinforcement bars. The proposed method and workflow are applicable to inspect and estimate these two types of reinforcement bars. In the target signal identification with YOLO v3, the GPR echo signals, whether reflected by round steel bars or ribbed steel bars, have the same hyperbolic shapes if they have the same cover thickness and diameter (Wiwatrojanagul et al., 2017). Although there exist slight differences in the reflected wave strength due to the different roughness of the steel bar surfaces, the identification of the hyperbolic signals is not influenced because YOLO v3 recognizes the reflected signals based on the geometric features of the hyperbolas. Therefore, the YOLO v3 network, which has been trained by the field GPR data, can be directly applied to the scenarios of round and ribbed steel bars without retraining. In the reinforcement bar estimation with 1D CNN, although the network is trained by the data calibrated by round steel bars, the corresponding algorithm and workflow can be extended to the estimation of ribbed steel bars, only if the calibration data are recollected from ribbed steel bars and the network is retrained. Theoretically, the same estimation accuracy can



be acquired. However, one of the potential challenges is that the unevenness of the ribbed steel bar surface requires high-precise experimental settings and elaborated operations when measuring the calibration data. Besides, the ribbed steel bars generally have three kinds of azimuthal distributions of ribs on the surface, that is, spiral shape, herringbone shape, and crescent shape (Zhu et al., 2018); and the steel bars with different models have different alloy compositions (A.R.C, 2010; Manera et al., 2008). The two aspects influence the intensity of the EMI responses to some extent. Therefore, special attention is to be paid to the following points: (1) the inspected ribbed steel bars should be ensured in strict conformance with the industrial manufacturing and processing standards and (2) their types and models should accord with those of the calibrated ribbed steel bars.

There are still some limitations on the practical applications of the current method. First, the conducted experiments present a single layer of reinforcement bars with considerable spacings between each other, where the adjacent bars have a negligible influence on the EM response of the target steel bars (Forde et al., 2013). However, in some realistic environments, there exist closely aligned, staggered, or welded reinforcement bars, where the measured EMI data cannot accord with the calibration EMI curves due to the interference from the other metal objectives or components. In principle, the proposed deep learning method has the potential to solve these complicated problems once the network is trained by sufficient sample data collected in the corresponding circumstances. However, extra prior knowledge is indispensable because more unknowns are involved. These considerations, in turn, require that in the on-site data collections of the current method, the measurement lines should be kept away from the welded and crosspoints. Second, the current work does not consider the corrosion of the reinforcement bars because the corrosion checking generally occurs in the late phase of construction rather than in the acceptance inspection phase (James et al., 2019). Corrosion of reinforcement bars has influence on the induced EM signals because the chemical components of the metal have changed. It is fairly worthy of investigating the quantitative relationship between the EM responses and the corrosion rate of the steel bars for assessing the quality of the old buildings.

Due to the limitation of the penetrating range of the instruments (see the statement in Section 2.1.1), the proposed method focuses on the applications in the residential buildings. However, the method and workflow can be extended to some similar NDT environments in civil and infrastructure engineering, typically exemplified by bridge pier, underground metal pipes, and pile foundation. In these scenarios, metallic annular or columnar objectives

are embedded in concrete or soil at a relatively large depth, and an instrument with deeper detection range are needed.

From the angle of algorithm development, the proposed deep learning algorithms can be further improved in the future work to cope with the identification and evaluation of reinforcement bars in the complicated scenarios mentioned above. The current study does not address the feature space that effectively characterizes the steel bar properties in the networks, which is actually important in improving the algorithms per se. In addition, it is worthy of investigating the feasibility of adopting some new deep learning algorithms in the current application. For example, neural dynamic classification, which can discover the most effective feature space, is especially valuable to investigate the fused data of reinforcement bars (Rafiei et al., 2017). Furthermore, a majority of deep learning algorithms adjust the hyperparameters through trials and errors, which is labor- and time-consuming. Some adaptive algorithms, such as dynamic ensemble learning, have the capability of automatically optimizing the hyperparameters of the designed networks during the training, which may be appealing for the NDT applications (Alam et al., 2020). From the view of the intelligent instrument development, the proposed deep learning algorithms are to be transplanted onto an embedded system small-size electronic board integrated by microprocessors, which will be convenient for a real-time testing and estimation on the site (Mittal, 2019).

## 5 | CONCLUSIONS

The current paper describes a deep learning-based strategy to evaluate the cover thickness and diameter of steel bars in reinforced concrete structures with combined GPR and EMI data. The proposed framework consists of two parts: (1) identification of hyperbolic signals in radargrams and (2) estimation of reinforcement bar diameter and cover thickness. In the hyperbolic signal recognition, a trained YOLO v3 network is used to identify target echo signals, which are characterized with hyperbolas, from radargrams collected in the residential buildings. The testing results show that  $F$ -score of YOLO v3 is 94.5%, AP is 94.8%, and AUC is 94.6%. Compared with the SSD method, YOLO v3 demonstrates a higher performance in identifying GPR hyperbolic signals. In the evaluation of reinforcement bar properties, a 1D CNN is trained with the EMI data calibrated in an in-house sand pit setup under the constraint of GPR estimated cover thickness range. The testing results show that under the permissible error of 1 mm, the estimation accuracy of the cover thickness and diameter of the reinforcement bars is 96.8% and 90.3%, respectively. Experiments with concrete specimens, which are configured by



22 estimated values of reinforcement bars, show that 17 values are accurately estimated and the error for the inaccurately estimated values is within 2 mm. The results further verify the effectiveness of the proposed method in reinforced concrete estimation. The study suggests that in the NDT and estimation of reinforcement bars, deep learning algorithms have the potentials of improving the efficiency of data processing and interpretations, and a well-trained deep learning network can take full advantage of the information contained in the multiple-source data to improve the estimation accuracy. Deep learning demonstrates great prospects in the NDT and estimation of civil and infrastructure engineering.

## ACKNOWLEDGMENTS

The research was funded by the National Natural Science Foundation of China (41974165, 42111530126) and Hubei Key Laboratory of Intelligent Geo-Information Processing (KLIIGIP-2018A2). The authors thank Zhiwei Duan and Xuefeng Yin for their contributions in the initial stage of the work, and the editor and anonymous reviewers for their constructive comments and suggestions to improve the quality of the paper.

## CONFLICT OF INTEREST

The authors declare no potential conflict of interests.

## REFERENCES

- Alam, K. M. R., Siddique, N., & Adeli, H. (2020). A dynamic ensemble learning algorithm for neural networks. *Neural Computing and Applications*, 32(12), 8675–8690.
- Allred, J. (1995). Improvement to the orthogonal method for determining reinforcing bar diameter using a cover meter. In M. Forde, *Proceedings of the Sixth International Conference on Structural Faults and Repair* (Vol. 2, pp. 11–15). Edinburgh: Engineering Technics Press.
- Amezquita-Sanchez, J. P., Valtierra-Rodriguez, M., Aldwaik, M., & Adeli, H. (2016). Neurocomputing in civil infrastructure. *Scientia Iranica*, 23(6), 2417–2428.
- A.R.C, S. (2010). *Smorgon ARC-reinforcement handbook: Your guide to steel reinforcement* (6th ed.). Sunshine, Victoria: Smorgon ARC.
- Barca, E., De Benedetto, D., & Stellacci, A. M. (2019). Contribution of EMI and GPR proximal sensing data in soil water content assessment by using linear mixed effects models and geostatistical approaches. *Geoderma*, 343, 280–293.
- Belli, K., Wadia-Fascetti, S., & Rappaport, C. (2008). Model based evaluation of bridge decks using ground penetrating radar. *Computer-Aided Civil and Infrastructure Engineering*, 23(1), 3–16.
- Bengio, Y., & LeCun, Y. (2007). Scaling learning algorithms towards AI. *Large-Scale Kernel Machines*, 34(5), 1–41.
- Bradley, A. P. (1997). The use of the area under the ROC curve in the evaluation of machine learning algorithms. *Pattern Recognition*, 30(7), 1145–1159.
- Chen, X. W., & Lin, X. (2014). Big data deep learning: Challenges and perspectives. *IEEE Access*, 2, 514–525.
- Chinchor, N., & Sundheim, B. M. (1993). Muc-5 evaluation metrics. In *Fifth Message Understanding Conference (MUC-5)*, Baltimore, Maryland, August 25–27, 1993.
- Chollet, F. (2017). *Deep learning with Python*. Simon and Schuster.
- Cortes, C., Mohri, M., & Rostamizadeh, A. (2012). L2 regularization for learning kernels. arXiv preprint arXiv:1205.2653.
- Dou, Q., Wei, L., Magee, D. R., & Cohn, A. G. (2016). Real-time hyperbola recognition and fitting in GPR data. *IEEE Transactions on Geoscience and Remote Sensing*, 55(1), 51–62.
- Feng, C., Liu, M.-Y., Kao, C.-C., & Lee, T.-Y. (2017). Deep active learning for civil infrastructure defect detection and classification. In K.-Y. Lin, *Computing in civil engineering 2017* (pp. 298–306). Seattle, Washington: ASCE.
- Forde, M., Hertlein, B., Basheer, M., Ferraro, C., Pessiki, S., & Bice, J. (2013). *Report on nondestructive test methods for evaluation of concrete in structures*. Report ACI Committee 228, American Concrete Institute, Farmington Hills, USA.
- Gao, Y., Ye, S., Zhang, X., & Fang, G. (2015). Novel detection system based on EMI and UWB. *Electronic Measurement Technology*, 38, 125–134.
- Giannakis, I., Giannopoulos, A., & Warren, C. (2020). A machine learning scheme for estimating the diameter of reinforcing bars using ground penetrating radar. *IEEE Geoscience and Remote Sensing Letters*, 18(3), 461–465.
- Guo, J., Wang, Q., & Li, Y. (2021). Semi-supervised learning based on convolutional neural network and uncertainty filter for façade defects classification. *Computer-Aided Civil and Infrastructure Engineering*, 36(3), 302–317.
- Hai, S., Wang, J., Wu, D., & Bao, Q. (2002). Evaluating the quality of project supervision engineers—A case study in China. *International Journal of Construction Management*, 2(1), 13–23.
- Hu, F., Zhao, J., Huang, Y., & Li, H. (2021). Structure-aware 3D reconstruction for cable-stayed bridges: A learning-based method. *Computer-Aided Civil and Infrastructure Engineering*, 36(1), 89–108.
- James, A., Bazarchi, E., Chiniforush, A. A., Aghdam, P. P., Hosseini, M. R., Akbarnezhad, A., Martek, I., & Ghodoosi, F. (2019). Rebar corrosion detection, protection, and rehabilitation of reinforced concrete structures in coastal environments: A review. *Construction and Building Materials*, 224, 1026–1039.
- Jazayeri, S., Kruse, S., Hasan, I., & Yazdani, N. (2019). Reinforced concrete mapping using full-waveform inversion of GPR data. *Construction and Building Materials*, 229, 117102.
- Jol, H. M. (2008). *Ground penetrating radar theory and applications*. Elsevier.
- Kim, M.-K., Thedja, J. P. P., Chi, H.-L., & Lee, D.-E. (2021). Automated rebar diameter classification using point cloud data based machine learning. *Automation in Construction*, 122, 103476.
- Kingma, D. P., & Ba, J. (2014). Adam: A method for stochastic optimization. arXiv preprint arXiv:1412.6980.
- Krizhevsky, A., Sutskever, I., & Hinton, G. E. (2017). Imagenet classification with deep convolutional neural networks. *Communications of the ACM*, 60(6), 84–90.
- Lai, W. W.-L., Derobert, X., & Annan, P. (2018). A review of ground penetrating radar application in civil engineering: A 30-year journey from locating and testing to imaging and diagnosis. *NDT & E International*, 96, 58–78.
- Leet, K., & Bernal, D. (1982). *Reinforced concrete design*, Vol. 384. McGraw-Hill.



- Lei, W., Hou, F., Xi, J., Tan, Q., Xu, M., Jiang, X., Liu, G., & Gu, Q. (2019). Automatic hyperbola detection and fitting in GPR B-scan image. *Automation in Construction*, *106*, 102839.
- Lin, M., Chen, Q., & Yan, S. (2013). Network in network. arXiv preprint arXiv:1312.4400.
- Liu, H., Lin, C., Cui, J., Fan, L., Xie, X., & Spencer, B. F. (2020). Detection and localization of rebar in concrete by deep learning using ground penetrating radar. *Automation in Construction*, *118*, 103279.
- Liu, H., Lu, H., Lin, J., Han, F., Liu, C., Cui, J., & Spencer, B. F. (2021). Penetration properties of ground penetrating radar waves through rebar grids. *IEEE Geoscience and Remote Sensing Letters*, *18*(7), 1199–1203.
- Liu, H., & Sato, M. (2014). In situ measurement of pavement thickness and dielectric permittivity by GPR using an antenna array. *NDT & E International*, *64*, 65–71.
- Maeda, H., Kashiyama, T., Sekimoto, Y., Seto, T., & Omata, H. (2021). Generative adversarial network for road damage detection. *Computer-Aided Civil and Infrastructure Engineering*, *36*(1), 47–60.
- Manera, M., Vennesland, Ø., & Bertolini, L. (2008). Chloride threshold for rebar corrosion in concrete with addition of silica fume. *Corrosion Science*, *50*(2), 554–560.
- Mittal, S. (2019). A survey on optimized implementation of deep learning models on the Nvidia Jetson platform. *Journal of Systems Architecture*, *97*, 428–442.
- Okazaki, Y., Okazaki, S., Asamoto, S., & Chun, P.-j. (2020). Applicability of machine learning to a crack model in concrete bridges. *Computer-Aided Civil and Infrastructure Engineering*, *35*(8), 775–792.
- Prego, F., Solla, M., Puente, I., & Arias, P. (2017). Efficient GPR data acquisition to detect underground pipes. *NDT & E International*, *91*, 22–31.
- Quek, S., Gaydecki, P., Zaid, M. A., Miller, G., & Fernandes, B. (2003). Three-dimensional image rendering of steel reinforcing bars using curvilinear models applied to orthogonal line scans taken by an inductive sensor. *NDT & E International*, *36*(1), 7–18.
- Rafiei, M. H., & Adeli, H. (2016). A novel machine learning model for estimation of sale prices of real estate units. *Journal of Construction Engineering and Management*, *142*(2), 04015066.
- Rafiei, M. H., Khushefati, W. H., Demirboga, R., & Adeli, H. (2017). Supervised deep restricted Boltzmann machine for estimation of concrete compressive strength. *ACI Materials Journal*, *114*(2), 237–244.
- Rathod, H., Debeck, S., Gupta, R., & Chow, B. (2019). Applicability of gpr and a rebar detector to obtain rebar information of existing concrete structures. *Case Studies in Construction Materials*, *11*, e00240.
- Redmon, J., Divvala, S., Girshick, R., & Farhadi, A. (2016). You only look once: Unified, real-time object detection. In *Proceedings of the IEEE conference on computer vision and pattern recognition* (pp. 779–788). Las Vegas, NV: IEEE.
- Redmon, J., & Farhadi, A. (2018). Yolov3: An incremental improvement. arXiv preprint arXiv:1804.02767.
- Ristic, A. V., Petrovacki, D., & Govedarica, M. (2009). A new method to simultaneously estimate the radius of a cylindrical object and the wave propagation velocity from GPR data. *Computers & Geosciences*, *35*(8), 1620–1630.
- Saey, T., Delefortrie, S., Verdonck, L., De Smedt, P., & Van Meirvenne, M. (2014). Integrating EMI and GPR data to enhance the three-dimensional reconstruction of a circular ditch system. *Journal of Applied Geophysics*, *101*, 42–50.
- Sajedi, S. O., & Liang, X. (2021). Uncertainty-assisted deep vision structural health monitoring. *Computer-Aided Civil and Infrastructure Engineering*, *36*(2), 126–142.
- Sami, A., & Abdulmunem, M. E. (2020). Synthetic aperture radar image classification: A survey. *Iraqi Journal of Science*, 1223–1232.
- Sato, M., Kikuta, K., & Miller, R. B. (2018). Evaluation of ALIS GPR for humanitarian demining in Colombia and Cambodia. In *2018 International Conference on Electromagnetics in Advanced Applications (ICEAA)*, (pp. 114–117). Cartagena, Colombia: IEEE.
- Sham, J. F., & Lai, W. W. (2016). Development of a new algorithm for accurate estimation of GPR's wave propagation velocity by common-offset survey method. *NDT & E International*, *83*, 104–113.
- Simonyan, K., & Zisserman, A. (2014). Very deep convolutional networks for large-scale image recognition. arXiv preprint arXiv:1409.1556.
- Slob, E., Sato, M., & Olhoeft, G. (2010). Surface and borehole ground-penetrating-radar developments. *Geophysics*, *75*(5), 75A103–75A120.
- Taheri, S. (2019). A review on five key sensors for monitoring of concrete structures. *Construction and Building Materials*, *204*, 492–509.
- Valikhani, A., Jaber Jahromi, A., Pouyanfar, S., Mantawy, I. M., & Azizinamini, A. (2021). Machine learning and image processing approaches for estimating concrete surface roughness using basic cameras. *Computer-Aided Civil and Infrastructure Engineering*, *36*(2), 213–226.
- Vélez, W., Matta, F., & Ziehl, P. (2016). Electrochemical characterization of early corrosion in prestressed concrete exposed to salt water. *Materials and Structures*, *49*(1), 507–520.
- Wang, Y., Cui, G., & Xu, J. (2020). Semi-automatic detection of buried rebar in GPR data using a genetic algorithm. *Automation in Construction*, *114*, 103186.
- Warren, C., & Giannopoulos, A. (2011). Creating finite-difference time-domain models of commercial ground-penetrating radar antennas using Taguchi's optimization method. *Geophysics*, *76*(2), G37–G47.
- Windsor, C. G., Capineri, L., & Falorni, P. (2013). A data pair-labeled generalized Hough transform for radar location of buried objects. *IEEE Geoscience and Remote Sensing Letters*, *11*(1), 124–127.
- Wiwatrojanagul, P., Sahamitmongkol, R., Tangtermsirikul, S., & Khamsemanan, N. (2017). A new method to determine locations of rebars and estimate cover thickness of RC structures using GPR data. *Construction and Building Materials*, *140*, 257–273.
- Wong, S. C., Gatt, A., Stamatescu, V., & McDonnell, M. D. (2016). Understanding data augmentation for classification: When to warp? In *2016 International Conference on Digital Image Computing: Techniques and Applications (DICTA)*, (pp. 1–6). IEEE.
- Xiao, P., Shi, Z., Wu, X., & Fang, G. (2017). Improved bucking coil design in helicopter transient electromagnetic system. *Progress in Electromagnetics Research M*, *60*, 131–139.
- Yosinski, J., Clune, J., Bengio, Y., & Lipson, H. (2014). How transferable are features in deep neural networks? arXiv preprint arXiv:1411.1792.
- Zaid, M., Gaydecki, P., Quek, S., Miller, G., & Fernandes, B. (2004). Extracting dimensional information from steel reinforcing bars in



- concrete using neural networks trained on data from an inductive sensor. *NDT & E International*, 37(7), 551–558.
- Zhang, J., Zhang, C., Lu, Y., Zheng, T., Dong, Z., Tian, Y., & Jia, Y. (2020). In-situ recognition of moisture damage in bridge deck asphalt pavement with time-frequency features of GPR signal. *Construction and Building Materials*, 244, 118295.
- Zhang, K., He, Z., Zheng, L., Zhao, L., & Wu, L. (2021). A generative adversarial network for travel times imputation using trajectory data. *Computer-Aided Civil and Infrastructure Engineering*, 36(2), 197–212.
- Zhang, R., Xu, J., Xu, J., Chen, S., & Cui, D. (2019). *Technical standard for test of reinforcing steel bar in concrete (in Chinese)*. China Architecture Publishing & Media Co., Ltd.
- Zhou, F., Chen, Z., Liu, H., Cui, J., Spencer, B. F., & Fang, G. (2018). Simultaneous estimation of rebar diameter and cover thickness by a GPR-EMI dual sensor. *Sensors*, 18(9), 2969.
- Zhou, X., Chen, H., & Li, J. (2018). An automatic GPR B-scan image interpreting model. *IEEE Transactions on Geoscience and Remote Sensing*, 56(6), 3398–3412.
- Zhu, J., Feng, C., Li, X., Zhang, W., & Dong, C. (2017). *China national standards GB-T 1499.1-2017. Steel for the reinforcement of concrete—Part 1: Hot rolled plain bars*. China National Standards.
- Zhu, J., Wang, L., Chen, J., Feng, C., & Yang, C. (2018). *China national standards GB-T 1499.2-2018. Steel for the reinforcement of concrete—Part 2: Hot rolled ribbed bars*. China National Standards.

**How to cite this article:** Li X, Liu H, Zhou F, Chen Z, Giannakis I, Slob E. Deep learning-based nondestructive evaluation of reinforcement bars using ground-penetrating radar and electromagnetic induction data. *Comput Aided Civ Inf*. 2021;1–20. <https://doi.org/10.1111/mice.12798>